Analyst

PAPER

View Article Online
View Journal | View Issue

Cite this: DOI: 10.1039/c4an01292e

An efficient technique for the reduction of wavelength noise in resonance-based integrated photonic sensors

Farshid Ghasemi, Maysamreza Chamanzar, Ali A. Eftekhar and Ali Adibi*

Received 16th July 2014
Accepted 30th August 2014

DOI: 10.1039/c4an01292e

www.rsc.org/analyst

A systematic study of the limit of detection (LOD) in resonance-based silicon photonic lab-on-chip sensors is presented. The effects of the noise, temperature fluctuations, and the fundamental thermodynamic limit of the resonator are studied. Wavelength noise is identified as the dominant source of noise, and an efficient technique for suppressing this noise is presented. A large ensemble of statistical data from the transmission measurements in a laser-scanning configuration on five silicon nitride (SiN) microrings is collected to discuss and identify the sources of noise. The experimental results show that the LOD is limited by a 3σ wavelength noise of ~1.8 pm. We present a sub-periodic interferometric technique, relying on an inverse algorithm, to suppress this noise. Our technique reduces the wavelength noise by more than one order of magnitude to an ensemble average of $3\sigma = 120$ fm, for a resonator quality factor (Q) of about 5×10^4 without any temperature stabilization or cooling. This technique is readily amenable to on-chip integration to realize highly accurate and low-cost lab-on-chip sensors.

1 Introduction

Recent progress in silicon (Si) photonics has led to novel and unique solutions for several applications including lab-on-chip sensing.[1–5] Nanophotonic devices provide a compact, low-cost, and sensitive transduction mechanism for bio/chemical sensing applications that can provide real-time sensing data without multi-step analyte handling or significant user intervention.[6,7] Resonant[8,9] and interferometric[2,10] lab-on-chip sensors have been employed for the on-chip detection of DNA,[11] microRNA,[12] toxins,[13] blood biomarkers,[14] and aptamers.[15] These devices rely on monitoring the refractive index perturbations induced by the target molecules to the sensing device. A higher sensor sensitivity is of interest as it allows the achievement of lower limits of detection (LOD). With increased sensitivity though, vulnerability to system noises and environmental fluctuations increases as well. This fact poses a continuous design challenge to identify and reduce (or compensate for) the undesired sources of uncertainty, in parallel to the efforts on the realization of more sensitive devices.

The bio/chemical sensor uncertainties can arise from device-level and system-level phenomena. For an on-chip resonance-based sensor, the resonance of a resonator shifts as a result of a change in the refractive index in the vicinity of the resonator. This shift is then used to sense and quantify the presence of target molecules. However, the presence of target molecules at the vicinity of the resonator is not the only reason for a resonance shift. A drift in temperature, for example, can lead to a similar resonance shift, practically indistinguishable from the one originated from the target molecules. For the suppression of the effect of temperature drift, several solutions including active temperature control,[2] athermal structures,[16] and on-chip differential referencing[17,18] have been proposed. Biochemical interference is another source of device-level noise, causing an ambiguity in relating the resonance shift to the presence of the target molecules.[19,20] To increase the specificity of the sensor and reduce biochemical interference, the surface of the sensing resonator is functionalized with selective receptor biomolecules to capture only the desired molecules.[21]

In contrast to the above-mentioned effects, the system-level uncertainties arise from the inaccuracies of optical interrogation system. For resonance-based integrated sensors, the employment of a tunable laser to scan the spectrum of the resonator is a conventional method for resonance tracking.[22] In this method, shot and thermal noises, either at the laser source or at the detector, are among the fundamental sources of amplitude noise.[23] Additionally, electronic noises and mechanical vibrations at the coupling points in the light path contribute to the random variations, not readily amenable to parametric modeling. Optical spectrum processing[24] and curve fitting[21,25] have been used to reduce these amplitude noises. In parallel, proper device and system designs help remove some unwanted spectral features such as Fabry–Perot oscillations. On the other hand, to reduce the inaccuracies in laser wavelength, precise wavelength measurement techniques have been proposed to correct for the wavelength deviations of tunable lasers.[22,26,27]

Department of Electrical and Computer Engineering, Georgia Institute of Technology, Atlanta, GA 30332, USA. E-mail: ali.adibi@ece.gatech.edu; farshid.ghasemi@gatech.edu

This paper investigates the sources of uncertainty in resonance detection for resonance-based lab-on-chip sensors using SiN microring resonators as the sensing device. Microring resonators have attracted extensive attention because of their simple structure and CMOS-compatible fabrication.[28,29] We present here a systematic and detailed statistical study of the experimental data from an array of SiN microring resonators to compare the relative significance of different sources of uncertainty. The measurement variations are shown to originate from the laser scan, and a simple and effective interferometric correction technique is proposed and demonstrated to suppress this noise by more than one order of magnitude down to $3\sigma \sim 120$ fm (wavelength error). Contrary to conventional fringe-counting methods, this technique takes advantage of the whole interferometric data to correct for sub-periodic wavelength deviations (*i.e.*, wavelength deviations much smaller than the spectral period of the interferometer). Our technique is simple, low-cost, suitable for on-chip integration, and excludes the use of active temperature controllers and high end wavemeters. The performance is studied across a relatively wide (6 nm) wavelength tuning range, as it is demanded in highly multiplexed sensing systems.

The structure of the article is as follows. In Section 2, we discuss device theory, fabrication, and experimental characterization setup. The sources of noise and their relative significance are discussed in Section 3. Based on these results, Section 4 is devoted to an effective wavelength measurement technique for the compensation of the dominant source of noise. The discussion of the results and final conclusions are summarized in Sections 5 and 6, respectively.

2 Microring resonators and optical system

2.1 Theory

For a microring resonator, the phase matching condition, implied by the periodic boundary condition of the structure for the azimuthal mode order m, results in[30]

$$\lambda_0 = \frac{2\pi r}{m} n_{\text{eff}}, \quad (1)$$

where λ_0 (resonance wavelength) depends linearly on the average microring radius (r), the effective index (n_{eff}), and inversely on azimuthal mode number (m). For each transverse mode (having a distinct effective index), various azimuthal modes differ in their m-numbers and form equally-distanced resonances in the spectral domain. This spectral spacing is referred to as the free-spectral range (FSR).

The binding of the target molecules to the resonator surface perturbs the effective index, resulting in a shift of the resonance wavelength. For an individual on-chip resonator with a linear response, sensing limit of detection (LOD) is defined as

$$\text{LOD} = \frac{3\sigma}{S}, \quad (2)$$

where S is the sensitivity, defined as the resonance shift divided by the input quantity (in terms of the thickness of a deposited monolayer, the bulk refractive index change of microring's cladding, or input analyte concentration); and σ is the standard deviation of the measured resonance shift without any input molecules. The LOD is the smallest quantity of the analyte that the sensor can detect its presence, within a confidence limit of 1%. As evident from eqn (2), the LOD is determined by measurement repeatability, quantified by σ.

Smaller LODs are achieved either by the enhancement of the device sensitivity (S), or through the improvement of detection accuracy (by reducing σ). Although an increase in the device sensitivity can compromise other system performance measures, such as multiplexing capability within a fixed bandwidth, an improvement in the detection accuracy does not cause such compromises. Our discussion throughout this paper examines the σ in eqn (2) for the resonance tracking of integrated photonic resonators. Spectrally multiplexed sensor arrays function over a relatively wide bandwidth including several multiplexed resonances. Hence, it is also important for a highly multiplexed sensor system to maintain its low LOD (*i.e.*, small σ) over a wide bandwidth.

2.2 Device design and nanofabrication

Fig. 1a shows the scanning electron micrograph (SEM) of a one-dimensional array of five microring resonators with a width of 500 nm and an outer radius of about 20 μm, serially coupled to a common bus waveguide with a widths of 500 nm. The resonance wavelengths of adjacent resonators differ by 0.25 nm, which is consistent with our design. Starting from a Si wafer, 4 μm thermal silicon oxide (SiO_2) was grown, and 240 nm stoichiometric SiN ($n = 2.05$) was deposited using low-pressure chemical vapor deposition (LPCVD). The device pattern was

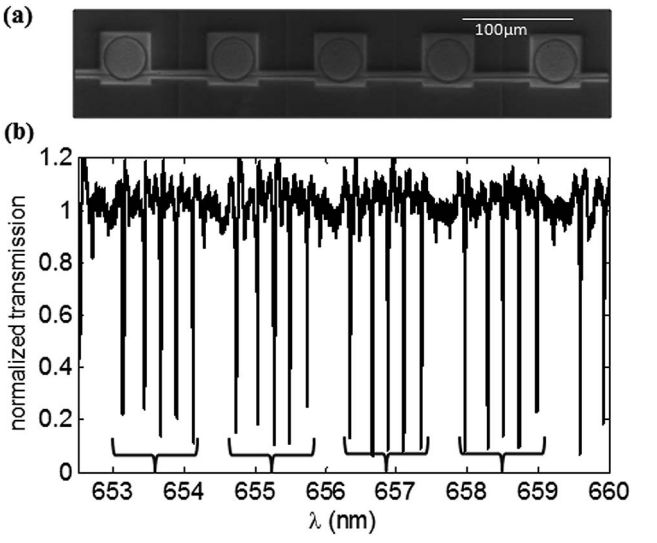

Fig. 1 (a) The SEM of five SiN microring resonators coupled to a bus waveguide. The width of each microring is 500 nm to ensure single-mode operation, and its radius is about 20 μm. (b) The experimental transmission spectrum of the device. Marked resonances are four azimuthal mode orders of the five microrings. The normalized transmitted spectrum is calculated by dividing the transmission power to the baseline. The baseline is obtained by low-pass filtering the transmission power.

written into ZEP520A electron-beam resist (from Zeon Corp.) by JEOL JBX-9300FS electron-beam lithography (EBL) system, and transferred into the SiN layer by inductively coupled plasma (ICP) etching using CF_4 chemistry, leaving no SiN pedestal. The residual resist was stripped using Microposit remover 1165 (Shipley). The device was then covered by a 2 μm layer of SiO_2 using plasma-enhanced chemical vapor deposition (PECVD) to exclude the effects of humidity or suspended particles in the air. The chip was finally cleaved to make waveguides accessible at the edges of the chip for input/output laser coupling.[13]

2.3 Optical system and data set

Coherent laser light from a tunable external cavity diode laser (652–660 nm, Newport TLB 6305) is conditioned by a half-wave plate, a polarizing beam splitter, and a lens to be coupled to the transverse magnetic (TM) mode of the waveguide on the chip (magnetic field in the device plane). The light transmitted through the waveguide is projected onto a photodetector by an output lens. The setup is controlled by LabView software to synchronously scan the laser wavelength (from 652 nm to 660 nm) and record the detector readout. Laser scan rate is 1 nm s^{-1}; and the spectrum sampling resolution is 20 fm. Normalized transmission spectrum is calculated by dividing the transmitted power (through the waveguide in Fig. 1a) to the baseline power. The baseline power is obtained by low-pass filtering the transmitted power to remove the resonance features of the spectrum.

The presence of five adjacent resonances is clear in Fig. 1b. From the repeated resonances, the FSR of the resonators is measured to be 1.65 nm, which is consistent with our finite-element simulations implemented in the COMSOL environment. We measured quality factors of 1.8×10^4 to 7.1×10^4 for the resonators, with an average of 5.4×10^4 and standard deviation of 1.4×10^4. This variation is primarily caused by fabrication imperfections. The spectrum of a single resonance is shown in Fig. 2. The transmission of the device is measured repeatedly 60 times without changing any experimental settings. We will use this ensemble for our statistical analysis in Sections 3 and 4.

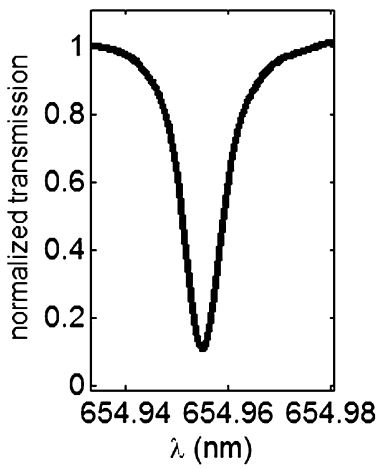

Fig. 2 Normalized transmission spectrum for a single resonance shown in Fig. 1. The linewidth is about 10 pm, and the Q is 6.5×10^4.

3 Noise sources

In this section, noise sources are discussed; and their effects on the repeatability of the resonance detection, *i.e.*, σ in eqn (2), are examined. The result of this examination will then be used to minimize the uncertainty in resonance detection.

3.1 Temperature effects

For integrated photonic devices, temperature fluctuations are among the most important environmental factors introducing undesired resonance drifts. In this regard, two distinct mechanisms should be distinguished from each other: (1) homogeneous temperature drifts; and (2) thermodynamic temperature fluctuations. On the one hand, the microrings are in contact with an environment with a time-dependent temperature. Thus, the temporal variations of average temperature lead to undesired resonance shifts. On the other hand, even if the average temperature is ideally stabilized, the temperature of the microring will fluctuate because of its finite volume. The temperature fluctuations of a microring in contact with a heat bath (*i.e.*, the second noise source mentioned above) can be evaluated according to the thermodynamics of this system.

The resonance wavelength drifts (with a standard deviation of $\sigma_{\lambda,T}$) originating from the homogeneous temperature drifts can be expressed in terms of average temperature drifts (with a standard deviation of σ_T) as[31]

$$\sigma_{\lambda,T} = \left(n_{\mathrm{eff}}\alpha_L + \frac{\partial n_{\mathrm{eff}}}{\partial T}\right)\frac{\lambda_0}{n_{\mathrm{g}}}\sigma_T. \quad (3)$$

Assuming a resonance wavelength (λ_0) of 655 nm, a group index (n_g) of 2.16; an effective index (n_{eff}) of 1.73 (from COMSOL simulations); $\partial n_{\mathrm{eff}}/\partial T$ of 2.4×10^{-5} K^{-1}, close to the thermo-optic coefficient (TOC) of SiN;[32] and an effective coefficient of thermal expansion (CTE or α_L) of $\simeq 2 \times 10^{-6}$ K^{-1};[33,34] the temperature sensitivity ($\sigma_{\lambda,T}/\sigma_T$) is about 8.3 pm K^{-1} according to eqn (3). Equivalently, from our finite-element calculations of the resonance wavelength of the microring resonators implemented in the COMSOL environment, assuming a TOC of 2.4×10^{-5} K^{-1} for SiN; a TOC of 1×10^{-5} K^{-1} for SiO_2;[32] and CTE of $\simeq 2 \times 10^{-6}$ K^{-1}; the temperature sensitivity is about 8.2 pm K^{-1}.

This type of temperature drift can be avoided by athermal designs that compensate the wavelength drifts originating from the thermo-optic effect in the core with that from the cladding and the substrate of the structure by employing materials with positive and negative TOCs, so that $\partial n_{\mathrm{eff}}/\partial T = 0$.[16,31,35] Another compensation technique is to use one or a subset of the microrings as reference. In doing so, each reference microring is isolated from the test solution by a protective layer.[17,18] The wavelength drifts of the reference microrings are attributed to the temperature variations and subtracted from the wavelength drifts in the sensing microring to compensate for the

homogeneous drifts. This differential resonance shift is not affected by a common drift in the temperatures of the microrings.

Although the average temperature drift can be compensated by athermal designs or differential measurements, such techniques do not help with the thermodynamic fluctuations of the temperature, where the contributions of different regions of the device (with either positive or negative TOC regions) are random variables adding up to form the overall resonance shift. The addition of these random variables will always result in an increased overall standard deviation, whether the TOCs are positive or negative. In this sense, SiN or SiO_2 resonators have an inherent advantage over Si resonators, because of their considerably smaller TOCs.

Thermodynamics sets a fundamental temperature noise floor for a microring in contact with a heat bath through the well-known equation[36]

$$\langle u^2 \rangle = \frac{\kappa T^2}{\rho C V}, \quad (4)$$

with κ, T, ρ, C, and V being the Boltzmann constant, absolute temperature, material density, specific heat capacity of resonator material, and mode volume, respectively. For SiN microrings studied here with $\rho = 3.3$ g cm^{-3}; $C = 7 \times 10^2$ J kg^{-1} K^{-1}; and $V \simeq 15$ μm^3; we will have fundamental thermal fluctuations of $\sqrt{\langle u^2 \rangle} \simeq 0.2$ mK at room temperature ($T = 300$ K). Hence, with a sensitivity of 8.3 pm K^{-1}, the corresponding fundamental thermorefractive noise in the system is $\sigma_{\lambda,T} \simeq 2$ fm at room temperature.

3.2 Amplitude noise

Ideally, we need as many data points as the number of model parameters to estimate the resonance lineshape and determine the resonance wavelength. Practically, two types of nonidealities hinder an accurate estimation: (1) random amplitude noises; and (2) the lack of an exact model for the system. While the former results in an uncorrelated noise on the sampled spectrum, the latter generates a correlated pattern in the measurements. Shot noise and thermal noise, either at the laser, at the detector, or at the electronics, are examples of such random noises.[37,38] Spectrum processing techniques, including denoising and the use of parametric fitting, have been used to reduce the random amplitude noise.[24,39] On the other hand, fabrication imperfections lead to resonance lineshape deformation, causing a correlated noise that can be most effectively removed by proper modeling. Examples of these deviations include Fabry–Perot oscillations and Fano-like resonance features,[40] added to the transmission spectrum because of fabrication imperfections introducing partial reflections.

The effect of random amplitude noises can be studied statistically by Monte Carlo simulations. We used a Lorentzian resonance with $Q = 5 \times 10^4$, an additive white Gaussian noise, and a sampling rate of 20 fm in our Monte Carlo simulations (with 10^4 iterations per data point), carried out similar to ref. 41. The generation of the Lorentzian resonance feature, the addition of the noise, and the determination of the resonance from the noisy resonance feature were performed in MATLAB. The ratio of the amplitude of the resonance feature (1 V) to the standard deviation of the noise is defined as the signal-to-noise ratio (SNR). To estimate the resonance wavelength from the noisy data, we used and compared three different algorithms. The first algorithm simply searches for the minimum of the noisy resonance feature. The second algorithm considers a window of 201 samples, selected symmetrically around the minimum point of the noisy resonance feature, and fits a quadratic polynomial to the data using linear regression. The third algorithm fits a Lorentzian function, within the same window as the second method, to find the resonance features. The results shown in Fig. 3 compare three resonance detection algorithms in terms of the standard deviations of detected resonance.

By performing multiple experimental measurements of microring resonances, the amplitude noise around the resonance wavelengths is measured to be few millivolts. Thus the experimental SNR is around 50 dB, for which the standard deviation of these three detection techniques are respectively, 176 fm, 7 fm, and 5 fm according to the Monte Carlo simulation (see Fig. 3). The difference between the quadratic fit and the Lorentzian fit becomes noticeable for higher SNRs, but for the working range of our experiment (with a SNR around 50 dB) a simple quadratic fit is sufficiently accurate and will be used. The expected ~7 fm variations of the resonance wavelength using a quadratic fit will be compared against the experimental level of noise in Section 3.4 to determine whether the noise mechanism discussed in this section can be the dominant noise factor in our setup.

3.3 Wavelength noise

Our measurement setup measures $\{\lambda, T(\lambda)\}$ samples, providing the transmission, $T(\lambda)$, at each wavelength, λ. Section 3.2 described the effect of the amplitude noises on $T(\lambda)$. This section looks into the wavelength noise on λ. In our setup, the LabView software instructs the laser controller to scan the wavelength with a fixed forward slew rate (r) in time (t) as

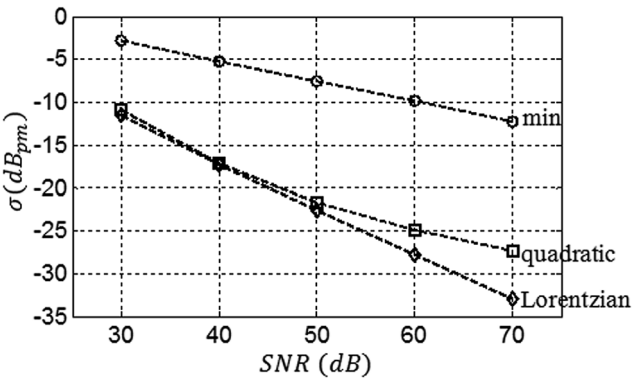

Fig. 3 Comparison of the performance of the three detection methods for different noise levels calculated using Monte Carlo simulations. dB_{pm} is defined as 10 log(σ/1 pm).

$$\lambda(t) = 652\ \text{nm} + r \times t, \tag{5}$$

while collecting the readout of the detector to form data points $\{\lambda(t_0),\ T(\lambda(t_0))\}$ at each time instant t_0. If the laser wavelength is off by $\delta_\lambda(t_0)$, the detector will record $T(\lambda(t_0) + \delta_\lambda(t_0))$, instead of $T(\lambda(t_0))$, in the absence of any other noises. This deviation can also be modeled as an equivalent amplitude noise of

$$\delta_T(t_0) = T(\lambda(t_0) + \delta_\lambda(t_0)) - T(\lambda(t_0)). \tag{6}$$

However, the conventional representation of this noise is in the form of a noise on the wavelength, and it is referred to as the spectral noise[41] or the wavelength noise.[42]

The prominent sources of wavelength noise in our setup are the phase noise of the laser; the inaccuracy of the tunable laser in setting the wavelength, resulting in a difference between the actual wavelength and the set wavelength of the laser at each time; and the jitter of analog-to-digital converter (ADC). Phase noise of the laser results in the broadening of the linewidth. Thus, the wavelength noise contribution from phase noise is on the order of the effective laser linewidth. The laser used in our setup has a linewidth of <300 kHz, which amounts to a wavelength noise of $\sigma_\lambda < 0.4$ fm. Practically, the laser linewidth is rarely the dominant limiting factor for the microring resonators discussed here considering typical ~100 kHz linewidths of existing commercial tunable lasers. For integrated photonic systems, hybrid on-chip Si photonic lasers have been demonstrated with a linewidth of 3.6 MHz, opening up the possibility for <MHz linewidths in near future.[43,44] Recent proof-of-concept demonstrations also indicate the possibility of kHz (*i.e.*, ~10 attometers) linewidths.[45]

At the above-mentioned linewidths, typically the variations induced by the tuning mechanism dominate the phase noise of the laser, especially where the tuning mechanism is mechanical or thermal. The external-cavity laser of this experiment uses Littman–Metcalf[46,47] configuration, which is commonplace for commercial external-cavity tunable lasers. The nominal wavelength tuning resolution of our laser is 20 pm.

3.4 Noise measurement

The measurement of σ (total standard deviations in the resonance wavelength) from the experimental data described in Section 2.3 helps evaluate the dominant source of noise. We use the differential resonance shifts here in order to remove the effect of temperature and other environmental drifts. This also eliminates the undesired scan-to-scan variations of the laser wavelength (*i.e.*, the variations of actual wavelength for a fixed set wavelength from one scan to another), although it does not compensate for within-scan variations (*i.e.*, the differential variations of actual wavelengths for any two set wavelengths in each scan). The total scan-to-scan variations were observed to be around 10 pm in the setup without differential resonance measurements. In order to compensate the scan-to-scan variations, we use the average of a number of neighboring resonances for each resonance as its reference resonance wavelength. The N_r neighboring resonances are selected such that the resonance of interest (indexed i) falls in the middle, *i.e.*, these neighbors range from $i - \lfloor N_r/2 \rfloor$ (closest integer smaller or equal to $N_r/2$) to $i + \lceil N_r/2 \rceil$ (closest integer larger or equal to $N_r/2$). We calculate the differential shift for the i-th resonance R_i as

$$\widetilde{R_i} = R_i - \frac{1}{N_r} \sum_{j=i-\lfloor N_r/2 \rfloor,\, j \neq i}^{i+\lceil N_r/2 \rceil} R_j. \tag{7}$$

Assuming the noises on the detected resonances to be independent and identically distributed random variables, the standard deviation of the i-th resonance referenced to its N_r neighboring resonances will be

$$\sigma(i, N_r) = \hat{\sigma}\sqrt{1 + \frac{1}{N_r}}, \tag{8}$$

where $\hat{\sigma}$ is the standard deviation of each detected resonance, originating from within-scan wavelength variations. We have plotted $\bar{\sigma}$, defined as: $\sigma(i, N_r)$ averaged over $i \in \{6, \ldots, 15\}$, in Fig. 4. Fitting eqn (8) to this plot determines individual deviations of $\hat{\sigma} = 410$ fm, which if accounted for by temperature only, corresponds to a temperature standard deviation of $\sigma_T \sim 0.2$ K. As the farthest resonators are located 400 μm apart on the chip and all are scanned in about 8 seconds, the observed resonance variations of 410 fm cannot be solely attributed to temperature changes, as it corresponds to a temporal temperature fluctuation of ~1 K s^{-1}, or a spatial temperature gradient of ~2 K mm^{-1}, which is very unlikely for the practical condition of our setup. On the other hand, as argued in Section 3.2 for the amplitude noise, the measured SNR in our system corresponds to resonance variations of ~7 fm using a quadratic polynomial fit. According to the nominal 20 pm accuracy of the laser in tuning the wavelength, we believe that the laser scan wavelength noise is the dominant source of noise. Thus, any effort to reduce this noise will result in considerable improvement in the sensor performance. The experiments and observations presented in the Section 4 will further support this claim.

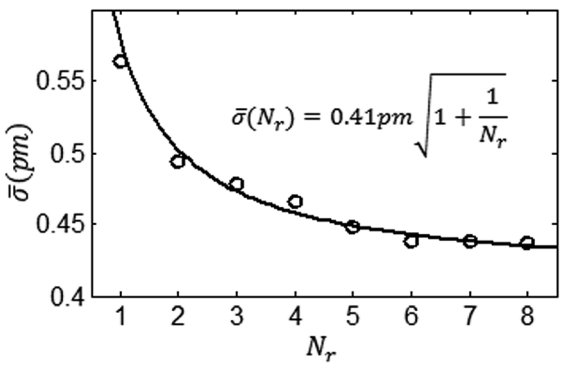

Fig. 4 Experimental referencing performance (the standard deviation in eqn (7)) for different number of reference resonances involved. The solid line is the fit according to the model in eqn (8).

4 Wavelength correction

In this section, we discuss an interferometric technique to monitor the wavelength and reduce the wavelength noise. The critical point in the resonance detection algorithm, where the dominant noise is added, is the assignment of pertinent wavelengths to the data points homogeneously sampled in time. This wavelength assignment is a projection from the time axis of the measurement to the wavelength axis, and we will refer to this projection as t–λ mapping.

To remove the wavelength noise, we measure a known and well-characterized spectral response simultaneously with our microring sensor, and use the inverse function of the spectral response to find the relative wavelengths. As shown in Fig. 5, we use a Michelson interferometer to meet this goal, although the method can work with any other device with a robust spectral response. As we are interested in the relative, rather than absolute, resonance shifts; the interferometer does not need any moving parts.[48,49]

The measurement of the transmission power of the device by detector D_1, and all the parameters of the measurement system (laser scan rate, sampling resolution, *etc.*) are similar to those explained in Section 2.3. The Michelson interferometer in Fig. 5 is designed to have a period of 1.58 pm. This period is chosen to be wide enough so that the system can densely sample the interferometer oscillations, but narrow enough to keep the detector noise of the interferometer much smaller than the interferometer peak-to-peak oscillations. Since analog-to-digital converter (ADC) samples are evenly spaced in time, a uniform wavelength scan is expected to result in a sinusoidal readout by the interferometer detector (D_2 in Fig. 5).

The wavelength difference among the data points is calculated using the inverse function of the sinusoidal response of the interferometer. This process is depicted in Fig. 6, where the wavelength offset, $\delta\lambda(t)$, relative to the closest peak (λ_n^{peak}), is

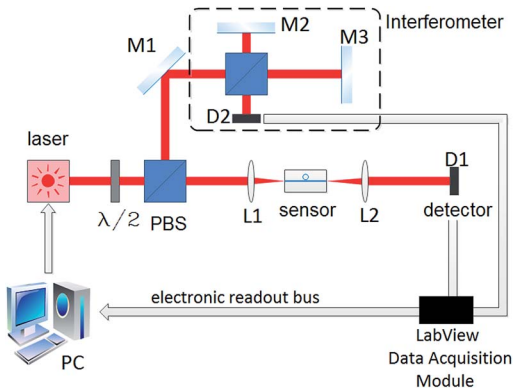

Fig. 5 Sensor characterization setup with a Michelson interferometer for the compensation of wavelength noise. After the polarizing beam splitter (PBS), the TM polarization is used as the input to the sensor chip, while the TE polarization is directed toward the Michelson interferometer. M denotes mirror; L, objective lens; D, detector; and $\lambda/2$, half-wave plate. The LabView module includes an analog-to-digital converter that samples the analog readout of the detectors D_1 and D_2, and sends the digitized samples to the personal computer (PC).

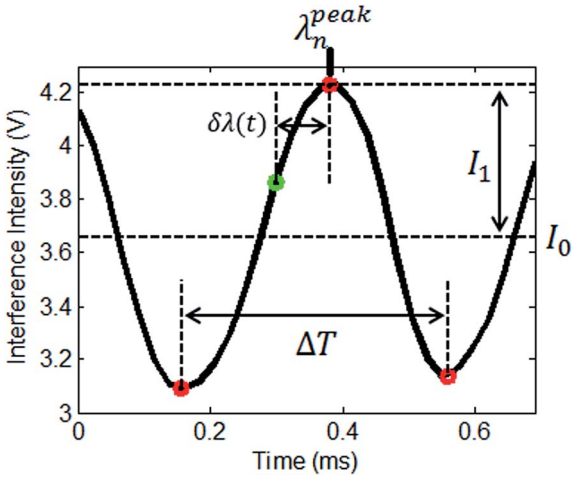

Fig. 6 Interferometer recording by detector D_2 in Fig. 5, from 0 to 0.7 ms. The parameters used in eqn (9) are marked on this figure. The amplitude data contains the wavelength deviation information.

$$\lambda(t) = \lambda_n^{\text{peak}} + \delta\lambda(t) = \lambda_n^{\text{peak}} \pm \Delta\lambda\left[\frac{1}{4} - \frac{1}{2\pi}\sin^{-1}\left(\frac{I(t)-I_0}{I_1}\right)\right], \quad (9)$$

in which $I(t)$ is the interferometer readout at time t, and $\Delta\lambda$ is the interferometer period in wavelength domain. The baseline (I_0) and local interferometer amplitude (I_1) are estimated by fitting a sinusoid locally to the data. The $\pm$ in eqn (9) refers to the temporal positioning of the data point after (for +) or before (for −) the closest peak (λ_n^{peak}). Eqn (9) provides the required inverse function for t–λ mapping.

Fig. 7 shows the experimental readout for forward slew rates (*i.e.*, scan speeds) of 0.5, 1, and 6 nm s^{-1}. A MATLAB code was prepared to identify and count all the interferometer peaks. The data from D_2 is smoothened by a 40-point moving average filter (about half the length of one interferometer period) and local maxima/minima are used to identify the interferometer periods. I_0 is calculated as the average of the amplitudes of the two closets extreme points (minima or maxima) points, and I_1 is calculated as the half the difference of the amplitudes of these two extreme points. Finally, the mapped wavelength for each data point is calculated using eqn (9). Each scan of the spectrum contains around 5000 interferometer peaks. The code was capable of recognizing the scans wherein one or more of these interferometer peaks were not successfully identified. This can happen because of a drastic deviation of the laser scan during one or few of the interferometer periods. Such scans, occurring in about 5% of the cases, were removed from this study as the code has been able to identify them *a priori*. To avoid the occurrence of such scans, the combination of two interferometers (with fine and coarse periods) and more complex pattern recognition algorithms can be used to increase the reliability.

Next, we experimentally investigate the efficiency of the t–λ mapping algorithm in reducing the wavelength noise of the sensor structure in Fig. 5. The resonances are studied in (R_i, R_j) pairs, where $|i - j| \neq 5$, 10, or 15 (to exclude the pairs

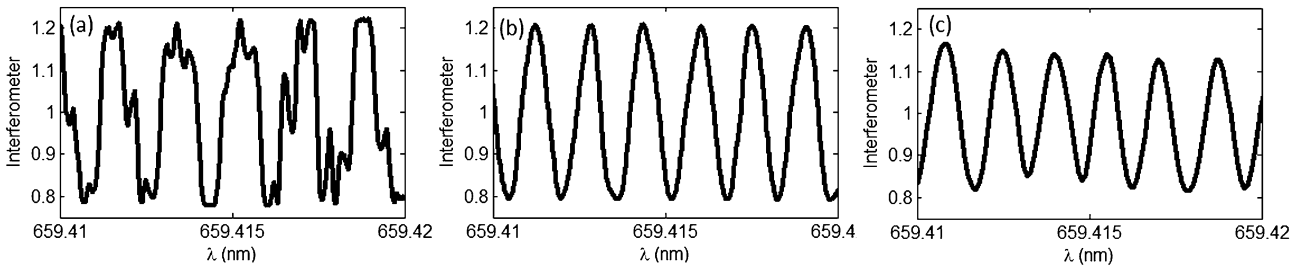

Fig. 7 The interferometer output of the setup in Fig. 5 (measured by D_2) for different laser scan speeds. Forward slew rates are (a) 0.5 nm s^{-1} (b) 1 nm s^{-1} (c) 6 nm s^{-1}. The parameter λ here shows the nominal set wavelength of the laser itself, calculated by a linear mapping from the time domain (*i.e.,* time instances at which the ADC samples the detectors) to wavelength domain, assuming that the laser scan is linear. A linear scan results in a sinusoidal interferometer output. The observed deviations in these figures from the expected sinusoid curve correspond to the deviations of the laser from the linear regime of scan. The deviations are random and these figures represent the typical amplitude of the deviations.

corresponding to different azimuthal modes of the same resonator). This provides us with $\binom{20}{2} - \frac{20\times 3}{2} = 160$ pairs in total, where $\binom{20}{2} = 20!/2!(20-2)!$. For each pair, the standard deviation Zof the spectral spacing $(R_i - R_j)$ is calculated over the ensemble of 60 measurements. A representative probability distribution function for two resonances, with $R_i - R_j = 5.097$ nm, is shown in Fig. 8a.

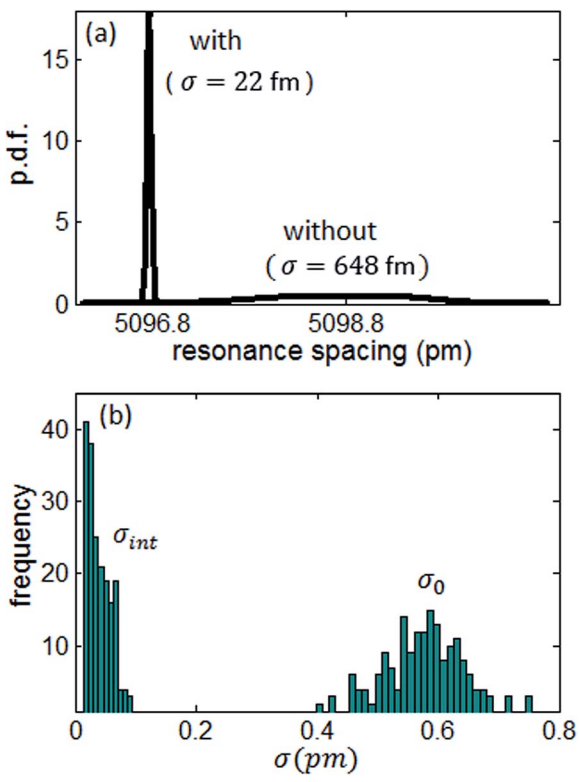

Fig. 8 Comparison of the standard deviation of resonance detection with and without t–λ mapping. (a) An example of the probability distribution functions for one of the pairs with an average resonance spacing of $R_4 - R_{20} = 5.097$ nm in the two cases. (b) The histograms of standard deviations with (σ_{int}) and without (σ_0) t–λ mapping.

The average over all 160 pairs using the interferometric technique is $\sigma_{\text{int}}^{\text{avg}} = 41$ fm, compared to $\sigma_0^{\text{avg}} = 585$ fm without the interferometer. The smallest standard deviation in this data set is 15 fm ($3\sigma_{\text{int}} = 45$ fm) corresponding to 11th and 13th resonances, $R_{13} - R_{11}$. The standard deviation of σ_{int} over the 160 resonance pairs is 19 fm. A histogram of the standard deviations for the resonance pairs, with and without the interferometric correction, is illustrated in Fig. 8b. The ability of the interferometer-based technique for reducing wavelength error is evident from Fig. 8.

We also calculated the statistical distribution of the improvement ratio (I.R.) in terms of standard deviations, *i.e.*

$$\text{I.R.} = \frac{{\sigma_0}^{(i,j)}}{{\sigma_{\text{int}}}^{(i,j)}}, \tag{10}$$

for above-mentioned (i,j) pairs of the resonances, where ${\sigma_{\text{int}}}^{(i,j)}$ and ${\sigma_0}^{(i,j)}$ denote the standard deviation of $R_i - R_j$ after correcting the wavelength with t–λ mapping, and that with simple linear mapping (without any correction). The improvement ratio has an average of ~18, a median of ~16, and a standard deviation of ~9. This clearly shows the power of our proposed correction technique in reducing the dominant noise factor in the sensor structure of Fig. 1a.

5 Discussion

Accurate resonance wavelength detection in resonator-based lab-on-chip sensors is a crucial step for achieving low LODs and reliable, repeatable performance. The results shown in Fig. 8 suggest that our t–λ mapping technique improves the detection accuracy of the sensor in Fig. 1a by more than one order of magnitude down to an average standard deviation of $3\sigma = 120$ fm, leading to an enhancement in the LOD by a similar factor. This observation reveals that the deviations in the initial system ($\sigma_0^{\text{avg}} = 585$ fm in Section 4, or equivalently, $\sqrt{2}\hat{\sigma} = 580$ fm from Section 3.1) were dominated by the wavelength noise of the laser. The results also demonstrate the possibility of achieving an accuracy of $3\sigma \sim 45$ fm (calculated from the 60 measurements of two specific resonances) using only one reference resonator and without cooling or temperature stabilization. The interferometer measurements are carried out in parallel to the

transmission measurements of the device, and the required data processing involves a moving-average filtering and few mathematical operations per data point. Thus, even using modest processors, our technique does not reduce the detection speed.

We did not use any temperature control or cooling for our measurements. Using a cooled and thermally stabilized fiber-based interferometer, with an FSR of 40.8 MHz, a repeatability of ~0.4 fm has been reported for microtoroids.[27] This accuracy, however, entails a temperature stabilization better than $\sim 1 \times 10^{-4}$ K for an SiO_2 microtoroid resonator. Our setup does not require any temperature control on the resonators or on the interferometer. Using thermal stabilizers in our system can improve the measurement accuracy, but such techniques add considerable complexity to the sensor and limit its practical application, especially in point-of-care and resource-limited settings. Furthermore, it has been the objective of this work to achieve accuracy homogeneously over a relatively wide bandwidth (here 6 nm), which is of interest for the applications requiring a high degree of spectral multiplexing. It should be mentioned that the use of high-end laboratory equipment might obviate the need for an interferometer, but increases the complexity, cost, and size of the system considerably.[50,51] Note that our technique can be readily used in many existing photonic resonance-based sensor chips to improve the detection limit by at least one order of magnitude without being limited to a specific resonator type, substrate material, or an interferometer configuration.

In another report, a 25 GHz Fabry–Perot etalon has been used as a wavelength reference to achieve a root-mean-square noise of 220 fm (*i.e.*, a 3σ noise 660 fm) for Si microrings.[22] The technique proposed here takes advantage of the amplitude of the interferometer readout at each data point to correct the associated wavelength deviation, as opposed to relying only on the data from the interferometer peaks. Therefore, this technique can correct for the sub-periodic deviations between the adjacent peaks. Such sub-periodic deviations are completely missed in the simple interpolation of the wavelength values measured only at the peaks.

Although we have used SiN microrings as the sensing resonators, the concept discussed here is applicable to other resonance tracking systems. The integrated version of this technique, *e.g.*, realized in the form of a Mach–Zehnder interferometer, benefits point-of-care and handheld bio/chemical sensing applications.[52] Furthermore, it allows for low-cost tunable lasers to scan the spectrum without requiring complex feedback circuitry for controlling the wavelength. In another aspect, our technique mitigates the issue of laser idle time in resonance-free bands of the spectrum. Adding a coarse interferometer (with a larger period), working in tandem with the fine interferometer used here, enables higher scan rates in resonance-free bands of the spectrum without loss of accuracy. As the internal configuration of the external cavity diode laser used here is one of the most widely used configurations in commercial lasers, we expect the conclusions here to be beneficial for other studies using similar setups. It should also be noted that because of its general nature, our technique can be applied to other on-chip resonance-based photonic sensors, such as photonic crystals and slot microrings.

To put the numbers from this study in a practical context, we discuss the specific case of cardiac biomarker detection for the diagnosis of heart failure. Cardiac troponin I (cTnI) is one of the most widely used blood biomarkers for the detection of myocardial injury.[53] For a typical sensitivity of ~100 pm nm^{-1} for the SiN microrings (*i.e.*, ~100 pm resonance shift for the deposition of a 1 nm layer with the refractive index of 1.45), a wavelength resolution of $3\sigma \simeq 120$ fm demonstrated here corresponds to an equivalent layer of about 1 pm thick, as the thinnest layer that the sensor is able to detect on its surface. Assuming a diameter of 4 nm for cTnI (the typical dimension of proteins with about 200 residues, as is the case for cTnI), a 1 pm layer on the SiN microring sensor amounts to the volume of about 4000 cTnI molecules. With a typical surface coverage of 10^{12} antibodies per cm^2,[54] about 10^6 antibody molecules will be available on the microring surface after antibody immobilization. As the smallest number of cTnI molecules on the surface that the sensor is able to sense is 4000, the smallest cTnI concentration that the sensor can sense is $4000/10^6 \times K_D$ (K_D is dissociation constant for cTnI/anti-cTnI). Assuming a dissociation constant in the nanomolar range (*i.e.*, $K_D \sim 1$ nM ~ 24 μg l^{-1}, as the molecular weight of cTnI is 24 kDa), the smallest cTnI concentration that this sensor can sense is ~0.08 μg l^{-1}. This detection limit is within the clinically relevant range for cTnI.[55,56] Therefore, using our proposed technique, clinically relevant concentrations of cTnI can be detected without the need to time-consuming sample preconcentration methods.[57] It should be noted that in order for the sensor system to take advantage of the wavelength correction technique discussed here, proper surface chemistry prohibiting non-specific binding should be used to avoid the dominance of biochemical noises in practice.[58] In this sense, the estimated value here (*i.e.*, LOD ~ 0.08 μg l^{-1}) will be a lower bound for the LOD of the complete sensor with the surface chemistry included.

6 Conclusion

A detailed study of noise sources in the laser-scanning setup for multiplexed integrated photonic sensors, which is a common configuration in many sensing scenarios, shows that the major source of noise is the inaccuracy of the laser in setting the wavelength. An efficient interferometric technique relying on sub-periodic wavelength correction was proposed and experimentally demonstrated to improve the detection accuracy by more than one order of magnitude from $3\sigma = 1.8$ pm to $3\sigma = 120$ fm (with σ being the standard deviations of measured resonance wavelength). This is the best reported repeatability at room temperature for the resonance detection of integrated microring and photonic crystal resonators to the best of our knowledge. Our technique is distinct from conventional interferometry techniques in its capability of sub-periodic wavelength correction enabled by the use of an inverse algorithm. The corresponding improvement in the LOD of the lab-on-chip sensors, by adding a simple interferometer without any temperature stabilization or cooling, is a main advantage of

our technique. In addition, it allows for the realization of lab-on-chip sensor systems having a low-cost on-chip tunable laser without complicated control circuitry. Thus, our technique can remarkably benefit bio/chemical lab-on-chip resonance-based integrated photonic sensor systems.

Acknowledgements

This work was supported by the Defense Advanced Research Projects Agency (DARPA) under Contract no. HR 0011-10-1-0075. The authors are thankful to Kerry Vahala and Kurt Wiesenfeld for fruitful discussions. They also thank Devin Brown for his help on EBL fabrication process; and Ehsan Shah Hosseini, Amir Hossein Atabaki, Mohammad Soltani, Qing Li, and Siva Yegnanarayanan for their help on fabrication process and optical characterization.

References

1 R. Soref, *IEEE J. Sel. Top. Quantum Electron.*, 2006, **12**, 1678–1687.
2 X. Fan, I. M. White, S. I. Shopova, H. Zhu, J. D. Suter and Y. Sun, *Anal. Chim. Acta*, 2008, **620**, 8–26.
3 U. Levy, K. Campbell, A. Groisman, S. Mookherjea and Y. Fainman, *Appl. Phys. Lett.*, 2006, **88**, 111107.
4 M. Sorel, G. Giuliani, A. Scirè, R. Miglierina, S. Donati and P. Laybourn, *IEEE J. Quantum Electron.*, 2003, **39**, 1187–1195.
5 W. D. Sacher, T. Barwicz, B. J. Taylor and J. K. Poon, *Opt. Express*, 2014, **22**, 3777–3786.
6 H. K. Hunt and A. M. Armani, *Nanoscale*, 2010, **2**, 1544–1559.
7 B. Kuswandi, Nuriman, J. Huskens and W. Verboom, *Anal. Chim. Acta*, 2007, **601**, 141–155.
8 R. Heideman, M. Hoekman and E. Schreuder, *IEEE J. Sel. Top. Quantum Electron.*, 2012, **18**, 1583–1596.
9 C.-Y. Chao, W. Fung and L. J. Guo, *IEEE J. Sel. Top. Quantum Electron.*, 2006, **12**, 134–142.
10 J. Xu, D. Suarez and D. S. Gottfried, *Anal. Bioanal. Chem.*, 2007, **389**, 1193–1199.
11 G. Rong, J. D. Ryckman, R. L. Mernaugh and S. M. Weiss, *Appl. Phys. Lett.*, 2008, **93**, 161109–161109.
12 A. J. Qavi and R. C. Bailey, *Angew. Chem.*, 2010, **122**, 4712–4715.
13 F. Ghasemi, A. A. Eftekhar, D. S. Gottfried, X. Song, R. D. Cummings and A. Adibi, *SPIE BiOS*, 2013, p. 85940A.
14 A. L. Washburn, M. S. Luchansky, A. L. Bowman and R. C. Bailey, *Anal. Chem.*, 2009, **82**, 69–72.
15 M. K. Park, J. S. Kee, J. Y. Quah, V. Netto, J. Song, Q. Fang, E. M. La Fosse and G.-Q. Lo, *Sens. Actuators, B*, 2013, **176**, 552–559.
16 K. B. Gylfason, C. F. Carlborg, A. Kazmierczak, F. Dortu, L. Vivien, C. A. Barrios, W. van der Wijngaart, G. Stemme, *et al.*, *Opt. Express*, 2010, **18**, 3226–3237.
17 J. T. Kirk, G. E. Fridley, J. W. Chamberlain, E. D. Christensen, M. Hochberg and D. M. Ratner, *Lab Chip*, 2011, **11**, 1372–1377.
18 L. Jin, M. Li and J.-J. He, *Opt. Commun.*, 2011, **284**, 156–159.
19 A. Hassibi, H. Vikalo and A. Hajimiri, *J. Appl. Phys.*, 2007, **102**, 014909.
20 Z. Mkhitaryan, A. Shatveryan, V. Aroutiounian, M. Ghulinyan, L. Pavesi, L. Kish and C. G. Granqvist, *Phys. E*, 2007, **38**, 160–163.
21 K. De Vos, J. Girones, T. Claes, Y. De Koninck, S. Popelka, E. Schacht, R. Baets and P. Bienstman, *IEEE Photonics J.*, 2009, **1**, 225–235.
22 M. Iqbal, M. A. Gleeson, B. Spaugh, F. Tybor, W. G. Gunn, M. Hochberg, T. Baehr-Jones, R. C. Bailey and L. C. Gunn, *IEEE J. Sel. Top. Quantum Electron.*, 2010, **16**, 654–661.
23 X. S. Yao and L. Maleki, *J. Opt. Soc. Am. B*, 1996, **13**, 1725–1735.
24 L. Chrostowski, S. Grist, J. Flueckiger, W. Shi, X. Wang, E. Ouellet, H. Yun, M. Webb, B. Nie and Z. Liang, *SPIE LASE*, 2012, p. 823620.
25 K. Kurihara, K. Nakamura and K. Suzuki, *Sens. Actuators, B*, 2002, **86**, 49–57.
26 F. Ghasemi and A. Adibi, *Conference on Lasers and Electro-Optics*, 2014, p. STh4H.4.
27 T. Lu, H. Lee, T. Chen, S. Herchak, J.-H. Kim, S. E. Fraser, R. C. Flagan and K. Vahala, *Proc. Natl. Acad. Sci. U. S. A.*, 2011, **108**, 5976–5979.
28 K. De Vos, I. Bartolozzi, E. Schacht, P. Bienstman and R. Baets, *Opt. Express*, 2007, **15**, 7610–7615.
29 J. S. Orcutt, A. Khilo, C. W. Holzwarth, M. A. Popović, H. Li, J. Sun, T. Bonifield, R. Hollingsworth, F. X. Kärtner, H. I. Smith, V. Stojanovic and R. J. Ram, *Opt. Express*, 2011, **19**, 2335–2346.
30 M. Soltani, S. Yegnanarayanan, Q. Li and A. Adibi, *IEEE J. Quantum Electron.*, 2010, **46**, 1158–1169.
31 J. Teng, P. Dumon, W. Bogaerts, H. Zhang, X. Jian, X. Han, M. Zhao, G. Morthier and R. Baets, *Opt. Express*, 2009, **17**, 14627–14633.
32 A. Arbabi and L. L. Goddard, *Opt. Lett.*, 2013, **38**, 3878–3881.
33 T. Retajczyk Jr and A. Sinha, *Thin Solid Films*, 1980, **70**, 241–247.
34 J.-H. Zhao, T. Ryan, P. S. Ho, A. J. McKerrow and W.-Y. Shih, *J. Appl. Phys.*, 1999, **85**, 6421–6424.
35 P. Alipour, E. S. Hosseini, A. A. Eftekhar, B. Momeni and A. Adibi, *Opt. Lett.*, 2010, **35**, 3462–3464.
36 M. L. Gorodetsky and I. S. Grudinin, *J. Opt. Soc. Am. B*, 2004, **21**, 697–705.
37 A. Yariv, *Introduction to optical electronics*, Holt, Rinehart and Winston, Inc., New York, NY, 1976.
38 X. Zhou, L. Zhang, A. Armani, D. Zhang, X. Duan, J. Liu, H. Zhang and W. Pang, *IEEE J. Sel. Top. Quantum Electron.*, 2014, **20**, 1–10.
39 P. Bienstman, K. De Vos, T. Claes, P. Debackere, R. Baets, J. Girones and E. Schacht, *Proc. SPIE*, 2009, 7220.
40 V. M. Passaro and F. De Leonardis, *IEEE J. Sel. Top. Quantum Electron.*, 2006, **12**, 124–133.
41 I. M. White and X. Fan, *Opt. Express*, 2008, **16**, 1020–1028.
42 J. Hu, X. Sun, A. Agarwal and L. C. Kimerling, *J. Opt. Soc. Am. B*, 2009, **26**, 1032–1041.

43 M. J. Heck, H.-W. Chen, A. W. Fang, B. R. Koch, D. Liang, H. Park, M. N. Sysak and J. E. Bowers, *IEEE J. Sel. Top. Quantum Electron.*, 2011, **17**, 333–346.
44 D. Liang and J. E. Bowers, *Nat. Photonics*, 2010, **4**, 511–517.
45 F. Aflatouni and H. Hashemi, *Opt. Lett.*, 2012, **37**, 196–198.
46 M. G. Littman and H. J. Metcalf, *Appl. Opt.*, 1978, **17**, 2224–2227.
47 S. Lecomte, E. Fretel, G. Mileti and P. Thomann, *Appl. Opt.*, 2000, **39**, 1426–1429.
48 J. Hall and S. Lee, *Appl. Phys. Lett.*, 1976, **29**, 367–369.
49 P. Fox, R. Scholten, M. Walkiewicz and R. Drullinger, *Am. J. Phys.*, 1999, **67**, 624.
50 Q. Quan, D. L. Floyd, I. B. Burgess, P. B. Deotare, I. W. Frank, S. K. Tang, R. Ilic and M. Loncar, *Opt. Express*, 2013, **21**, 32225–32233.
51 V. Dantham, S. Holler, V. Kolchenko, Z. Wan and S. Arnold, *Appl. Phys. Lett.*, 2012, **101**, 043704–043704.
52 L. Gervais, N. De Rooij and E. Delamarche, *Adv. Mater.*, 2011, **23**, H151–H176.
53 F. S. Apple and P. O. Collinson, *Clin. Biochem.*, 2012, **58**, 54–61.
54 P. Peluso, D. S. Wilson, D. Do, H. Tran, M. Venkatasubbaiah, D. Quincy, B. Heidecker, K. Poindexter, N. Tolani, M. Phelan, *et al.*, *Anal. Biochem.*, 2003, **312**, 113–124.
55 P. A. Kavsak, A. R. MacRae, M.-J. Yerna and A. S. Jaffe, *Clin. Biochem.*, 2009, **55**, 573–577.
56 S. Konstantinides, A. Geibel, M. Olschewski, W. Kasper, N. Hruska, S. Jäckle and L. Binder, *Circulation*, 2002, **106**, 1263–1268.
57 R. Kwak, S. J. Kim and J. Han, *Anal. Chem.*, 2011, **83**, 7348–7355.
58 A. Qureshi, Y. Gurbuz and J. H. Niazi, *Sens. Actuators, B*, 2012, **171**, 62–76.

